

Aerodynamic Shape Optimization of a Supersonic Transport Considering Low-Speed Stability

Sabet Seraj* and Joaquim R. R. A. Martins[†]
University of Michigan, Ann Arbor, Michigan 48109

Designing supersonic transport aircraft requires accounting for performance and stability and high-speed and low-speed conditions. Previous work demonstrated that there is a trade-off between high-speed performance and low-speed stability. Numerical optimization presents the opportunity to obtain the best high-speed performance while enforcing stability at low speeds. We perform RANS-based aerodynamic shape optimization with a component-based geometry parameterization approach that enables the optimization of a complex three-surface supersonic transport configuration. We minimize drag at a supersonic cruise condition both with and without a constraint on subsonic pitch stability. The stability constraint enforces a 5% static margin at a subsonic takeoff condition. We show that shape optimization increases the wing thickness and leading edge radius to design a cranked arrow wing that is stable at subsonic speeds at the cost of a 5.8% increase in supersonic drag.

I. Introduction

Supersonic transport (SST) aircraft must be designed with high-speed and low-speed flight regimes in mind. Efficiency and stability across different flight conditions are often competing objectives. For example, double delta or cranked arrow wings are known for providing a balance between supersonic and transonic performance. However, the same wings often exhibit inadequate pitch stability at low-speed, high angle of attack conditions [1]. Designing for subsonic stability is complicated by the leading edge vortices that are characteristic of flow over highly swept wings at high angles of attack [2].

The three main contributors to the pitch-up of cranked arrow wings are leading edge vortex effects, outboard flow separation, and vortex breakdown [3]. The wing planform is critical for the performance and stability of SST designs [1, 3], but the airfoil shape also has a strong influence on the leading edge vortex. Kulfan [4, 5] observed that greater wing thickness delays the growth of leading edge vortices and increases pitch stability. Similarly, Nelson [1] found that blunt leading edges and increased leading edge thickness delay subsonic pitch-up at the cost of increased supersonic wave drag. This represents a fundamental trade-off in SST design.

Computational fluid dynamics (CFD) combined with numerical optimization presents the opportunity to resolve flow features across different flight conditions and capture the trade-offs between competing design objectives. Several authors have demonstrated the value of applying multipoint optimization to supersonic aircraft. Cliff et al. [6] minimized a weighted sum of the thrust required for an SST design at supersonic and transonic conditions using the Euler equations as the aerodynamic model. Carrier [7] also used the Euler equations in minimizing the supersonic and transonic drag for an SST where the drag at the two conditions were equally weighted. More recent work has turned to the Reynolds-averaged Navier–Stokes (RANS) equations instead of the Euler equations. Bons et al. [8] performed aerostructural optimization of a supersonic business jet where the objective was to maximize a weighted sum of the supersonic and transonic range. Mangano and Martins [9] optimized the shape of a trapezoidal wing considering drag at subsonic, transonic, and supersonic Mach numbers. Despite considering multipoint performance trade-offs, none of these papers considered stability in the optimization problem.

A few papers have included low-speed constraints in the optimization of supersonic configurations, albeit with lower-fidelity methods. Dudley et al. [10] performed aerodynamic and structural optimization to minimize the takeoff gross weight of an SST subject to practical design constraints. Some of these were low-speed constraints such as limiting the angle of attack at landing and preventing engine scrape at landing. In a follow-up paper, Crisafulli et al. [11] augmented the vortex-lattice method used for stability derivative computation in their framework with a pitch-up estimation method [3] to capture nonlinear pitch-up characteristics in the model. However, subsonic pitch stability was not included as a constraint in either of these two papers. The papers also primarily looked at planform effects and

*Ph.D. Candidate, Department of Aerospace Engineering. Student Member AIAA.

[†]Professor, Department of Aerospace Engineering. Fellow AIAA.

lacked the fidelity and scalability for detailed airfoil shape parameterization. More recently, Li and Geiselhart [12, 13] optimized an SST using a sequence of optimization problems to enforce low-boom constraints and mission constraints, including static margin requirements at landing and takeoff (LTO). However, the LTO analysis was done using a linear aerodynamic code. In addition, they did not explicitly consider subsonic pitch-up or the trade-off between supersonic performance and subsonic stability.

The goal of this paper is to use RANS-based optimization to study the effect of aerodynamic shape on the subsonic pitch stability of an SST and to quantify the supersonic drag penalty associated with enforcing a subsonic stability constraint. We first describe the aircraft geometry and evaluate the accuracy of RANS at low-speed, high angle of attack conditions in Sec. II. We then present the optimization formulation and optimized aircraft designs in Sec. III.

II. Validation at Subsonic Conditions

A. Aircraft geometry

The aircraft we are interested in is an SST with a cranked arrow wing, a T-tail, and a canard (Fig. 1). This configuration was designed by the University of Washington as a baseline model to study the low-speed characteristics of SSTs [14, 15]. A major part of this effort involves wind tunnel testing at subsonic conditions. We use the wind tunnel data for this configuration to check whether our aerodynamic model is suitable for the low-speed, high angle of attack flows relevant for the subsonic pitch-up of supersonic aircraft. The flight scale dimensions for the wing are listed in Table 1. This is the scale we use for the optimizations in Sec. III. The wind tunnel model is scaled down by a factor of 22. The reference point for the pitching moment is at 25% of the mean aerodynamic chord.

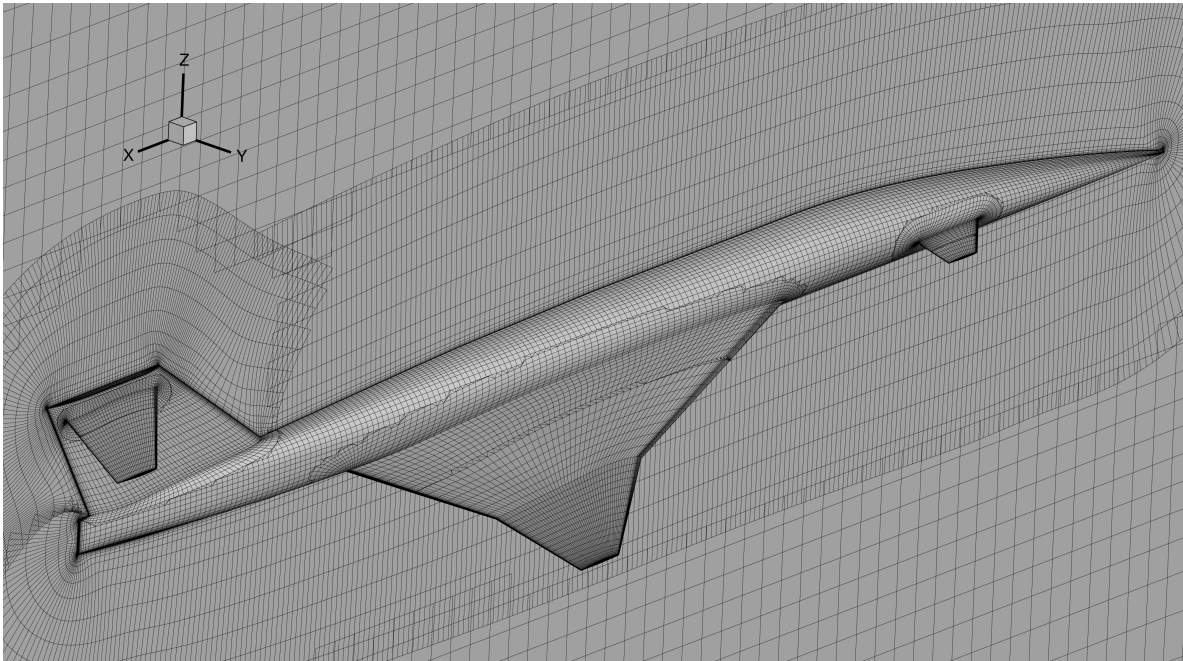


Fig. 1 Coarse overset mesh of the supersonic transport configuration considered in this work

B. CFD solver and meshes

The CFD solver we use is ADflow [16], a finite volume code for multiblock and overset structured meshes. We use ADflow to solve the compressible RANS equations with the Spalart–Allmaras (SA) turbulence model [17]. We generate an overset mesh for the aircraft by first creating multiblock component and collar surface meshes [18] using Ansys ICEM CFD. We then extrude the surface meshes to generate volume meshes using pyHyp [19], a hyperbolic mesh generation code based on the work of Chan and Steger [20]. Finally, we combine the component meshes with a background mesh to form the complete overset mesh. The background mesh consists of a Cartesian mesh in the overlapping region near

Table 1 Flight scale wing dimensions

Quantity	Value
Reference area	373.03 m ²
Mean aerodynamic chord	14.565 m
Half-span	14.760 m

the aircraft, surrounded by a hyperbolic O-mesh. The farfield boundary of the O-mesh extends to 50 times the mean aerodynamic chord away from the Cartesian region. We use a zipper mesh approach [21] to account for overlapping regions on the surface mesh when computing integrated quantities such as drag. The total number of cells and the number of compute cells after implicit hole cutting [22] for the two overset meshes used in the validation study are listed in Table 2. The coarse overset mesh, shown in Fig. 1, is a uniformly coarsened version of the fine mesh.

Table 2 CFD mesh characteristics

Mesh	Total cells	Compute cells
Coarse	1 388 079	1 103 797
Fine	11 104 632	8 982 120

C. Comparison between RANS and experimental data

Figure 2 shows a comparison between RANS results and wind tunnel data for angles of attack from -10 deg to 25 deg. For RANS, we use a Reynolds number based on the mean aerodynamic chord of 2.4 million and a Mach number of 0.16. These are both slightly higher than the wind tunnel condition, where the Reynolds number is around 2.2 million and the Mach number is around 0.15. To simplify the overset meshing, we exclude a small wing-fuselage fairing that is present in the wind tunnel model.

All RANS solutions are converged to a total residual of 10^{-7} or tighter relative to the freestream residual. The fine mesh provides an excellent match for the lift and drag across the entire angle of attack range. The coarse mesh is nearly as accurate from -10 to 10 deg but is slightly less accurate at higher angles of attack. The discrepancies between the experiment and CFD are most pronounced for the pitching moment. However, we are mostly interested in capturing the shape of the pitching moment curve, especially around the pitch-up angle, because this determines the pitch stability of the aircraft. The fine mesh predicts the shape of the pitching moment accurately up to 15 deg, which includes the pitch-up onset. The coarse mesh has a similar shape as the fine mesh but underpredicts the pitch-up angle by about one degree. Overall, the coarse mesh provides reasonable accuracy at about 3% of the computational cost of the fine mesh. Therefore, we use the coarse mesh for all optimizations.

III. Aerodynamic Shape Optimization

The framework we use to perform aerodynamic shape optimization is MACH-Aero[‡]. MACH-Aero has been used extensively for aerodynamic shape optimization of wings and full aircraft configurations [23]. We briefly describe each component of the framework here. As described in Sec. II, we use ADflow as the CFD solver. We converge the RANS equations to a total residual of 10^{-8} relative to freestream using the approximate Newton–Krylov startup strategy [24] and then switch to an exact Newton–Krylov solver to converge to a relative residual of 10^{-10} . The discrete adjoint implementation in ADflow allows for efficient computation of gradients with respect to many design variables [25].

We parameterize the geometry using free-form deformation (FFD) [26], implemented in pyGeo [27]. We use a component-based approach to deform the surface mesh, which we present in Sec. III.B. The changes to the surface mesh are propagated through the volume mesh using an inverse distance mesh deformation algorithm [28], implemented in IDWarp [19]. Both pyGeo and IDWarp are differentiated so that they can be used in gradient-based optimization.

[‡]<https://github.com/mdolab/MACH-Aero>

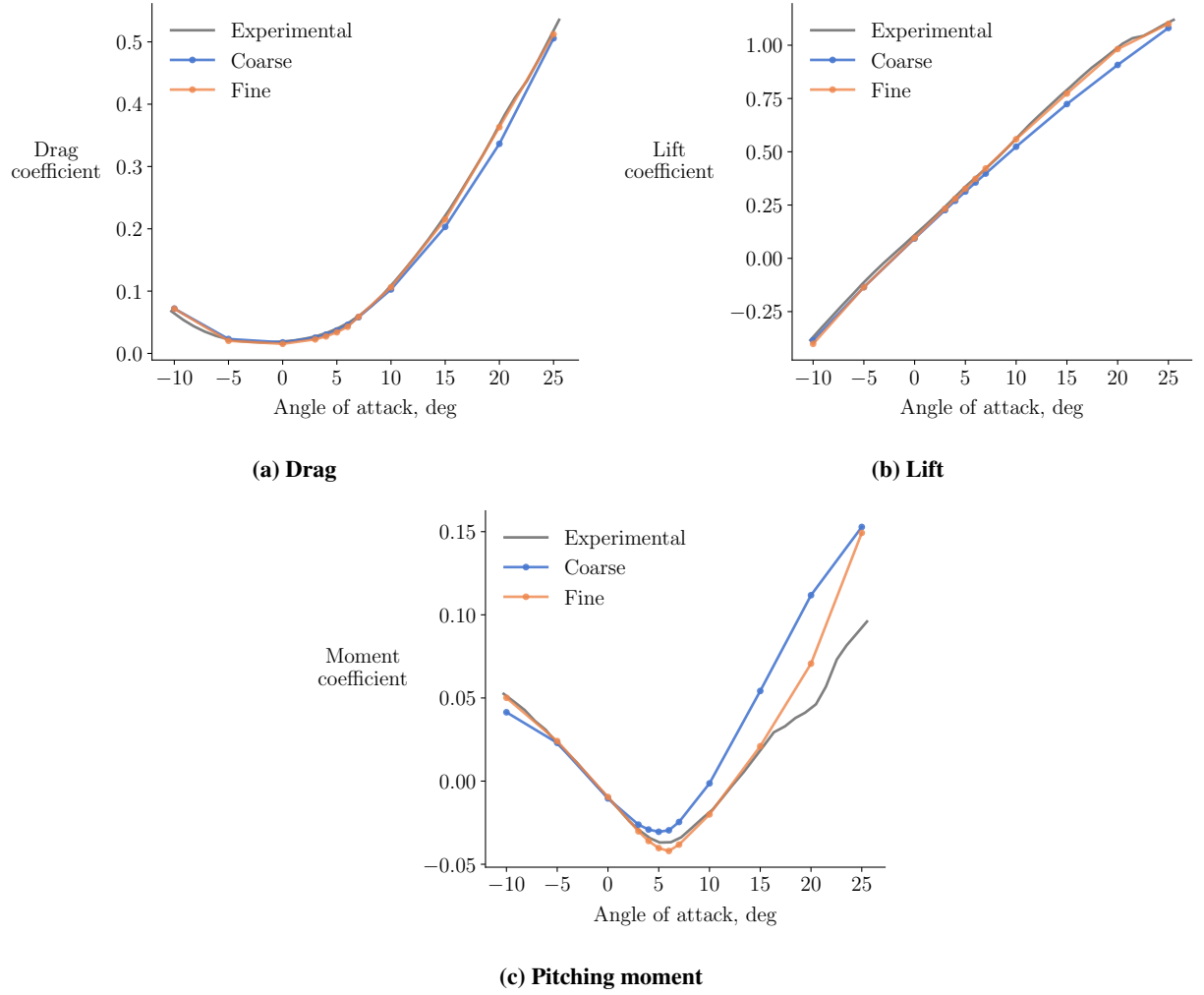


Fig. 2 Comparison of ADflow force and moment coefficients with experimental data

For the optimization, the analysis and gradient computation are wrapped with pyOptSparse [29], which provides a Python interface to different optimizers. The optimizer we use is SNOPT [30], a sequential quadratic programming algorithm designed for large-scale problems.

A. Optimization problem

We are interested in evaluating the supersonic drag penalty associated with enforcing a subsonic stability constraint. To formulate this optimization problem, we first define a supersonic cruise condition and a subsonic takeoff condition in Table 3. The flight conditions and their corresponding lift coefficients are based on flight envelopes and weight estimates from previous SST studies by Boeing [31] and Lockheed Martin [32]. The target static margin, K_n^* , is used to define the subsonic stability constraint.

Table 3 Flight conditions

	Mach number	Altitude, m	Altitude, ft	Reynolds number	C_L^*	K_n^*
Supersonic	1.8	16764	55000	101.8×10^6	0.2	
Subsonic	0.3	0	0	80.4×10^6	0.7	5%

We run two supersonic drag minimization problems: one without a subsonic stability constraint and one with a subsonic stability constraint. The optimization formulation with the stability constraint is shown in Table 4. Each flight condition has separate angle of attack, tail rotation, and canard rotation variables to trim the aircraft. For the moment computation, we assume that the center of gravity (CG) is fixed at 25% of the mean aerodynamic chord. The wing design variables are shared across the supersonic and subsonic conditions. For the optimization without the subsonic stability constraint, the subsonic design variables and constraints are excluded from the optimization problem. We further discuss the geometric design variables and constraints in Sec. III.B and the stability constraint in Sec. III.C.

Table 4 Supersonic drag minimization with subsonic static margin constraint

		Quantity	Lower	Upper	Scaling
Minimize	$C_{D, \text{supersonic}}$	1			100
With respect to	Angle of attack	2	-5°	20°	0.1
	Tail rotation	2	-9°	9°	0.1
	Canard rotation	2	-5.5°	13.5°	0.1
	Wing twist	7	-10°	10°	0.1
	Wing sectional shape	112	-2 m	2 m	1
	Wing vertical displacement	1	0 m	0.1 m	1
Total number of design variables		126			
Subject to	$C_L \div C_L^*$	2	1	1	1
	C_M	2	0	0	1
	$K_n \div K_n^*$	1	1		0.1
	Wing thickness \div Baseline wing thickness	100	1		1
	Wing volume \div Baseline wing volume	1	1		1
	No shear at wing leading and trailing edges	14			
Total number of constraints		120			

B. Component-based geometry parameterization

To parameterize the geometry, we split the aircraft into five components: the fuselage, wing, canard, horizontal stabilizer, and vertical stabilizer. We define FFD volumes for each component, shown in Fig. 3a. The black spheres are FFD control points, and the blue spheres are reference axis control points. The reference axes are used to define design variables that act on groups of FFD control points. The horizontal stabilizer and canard reference axes are used to define the tail and canard rotation variables, respectively. Both rotation variables rotate the entire component about the mid-chord. The wing reference axis is used to define the twist variables, each of which rotates one spanwise section of the wing about the trailing edge, and the vertical displacement variable, which moves the entire wing in the z -direction. The wing shape variables are defined by the movement of individual FFD control points in the z -direction. The twist and shape variables are defined at all sections other than the wing root, which is located inside the fuselage. The thickness and volume constraints ensure that the optimized wing is not unrealistically thin. The thickness constraints are applied on a 10×10 grid of points across the wing planform. In addition, we apply linear constraints at the leading and trailing edge FFD control points to prevent shear deformations. The fuselage and vertical stabilizer FFD volumes are stationary but are needed to define and preserve the shape of their respective components.

Away from intersections, the changes to the CFD surface mesh are defined solely by the FFD. Near component intersections, we use the surface mesh deformation method developed by Yildirim et al. [33] to maintain a valid CFD mesh. This method relies on triangulated surface meshes (Fig. 3b) and the pySurf module of Secco et al. [34] to compute intersections between components, perform projections, and remesh curves. Table 5 lists the number of nodes and triangles in each triangulated surface we use. The triangulated surfaces are refined in regions of high curvature and near component intersections.

Table 5 Triangulated surface characteristics

Component	Nodes	Triangles
Fuselage	240 503	478 906
Wing	96 162	191 239
Canard	58 348	116 443
Horizontal stabilizer	35 720	70 978
Vertical stabilizer	31 472	62 234

We demonstrate the effectiveness of the component-based parameterization using the tail rotation as an example. Figure 4 shows the T-tail surface mesh at the lower and upper bounds of the tail rotation variable. We obtain a valid mesh for rotation angles from -9 deg to $+9$ deg. In addition, the vertical stabilizer's shape is preserved even after applying large rotations to the horizontal stabilizer.

C. Subsonic stability constraint

The stability constraint enforces a static margin of at least 5% at the subsonic condition. We derive the equation for the static margin by starting from the definition of the moment coefficient about the CG ($C_{M_{CG}}$) in terms of the moment coefficient about the neutral point ($C_{M_{NP}}$):

$$C_{M_{CG}} = C_{M_{NP}} + C_L \cos \alpha (h_{CG} - h_{NP}) + C_D \sin \alpha (h_{CG} - h_{NP}), \quad (1)$$

where h_{CG} and h_{NP} are the longitudinal locations of the CG and the neutral point, respectively, normalized by the mean aerodynamic chord. Substituting the definition of the normal force coefficient

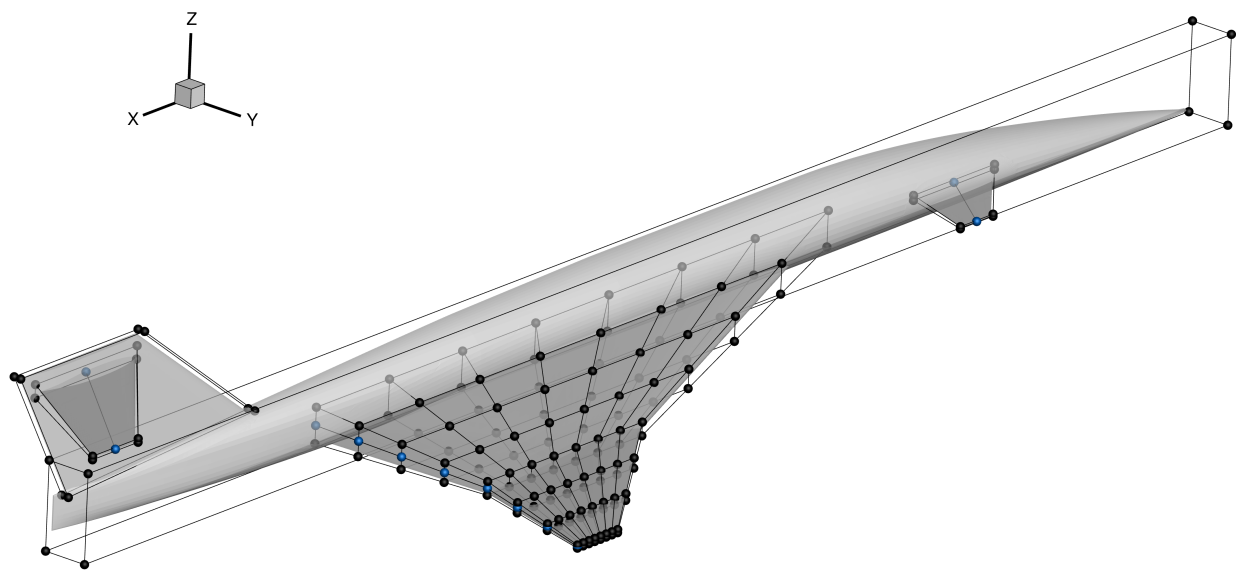
$$C_N = C_L \cos \alpha + C_D \sin \alpha, \quad (2)$$

we have

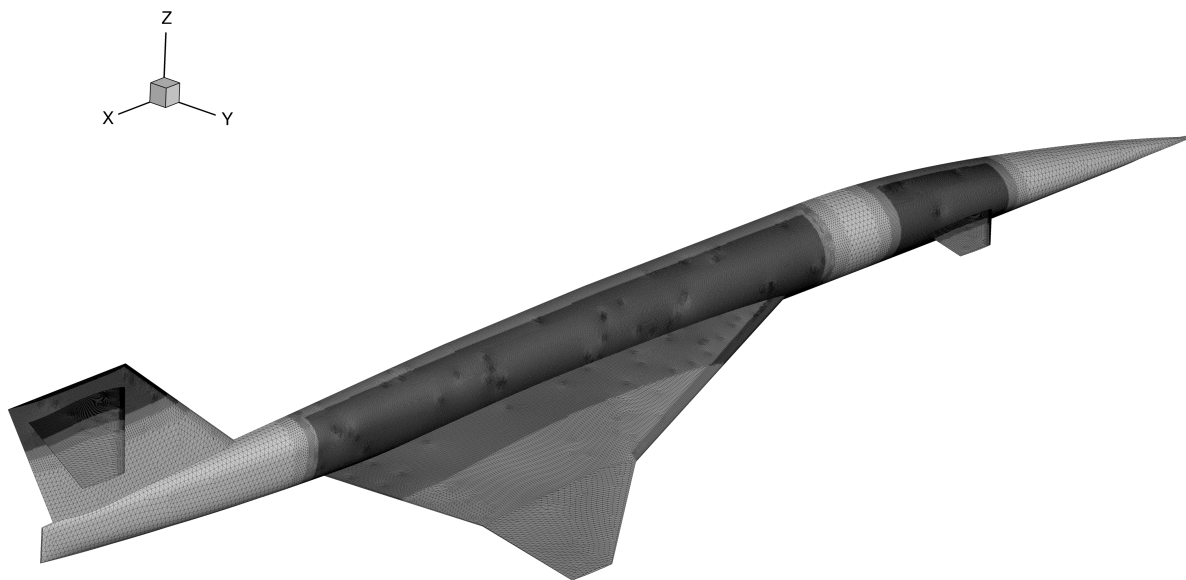
$$C_{M_{CG}} = C_{M_{NP}} + C_N (h_{CG} - h_{NP}). \quad (3)$$

Taking the derivative with respect to α gives

$$C_{M_\alpha} = C_{N_\alpha} (h_{CG} - h_{NP}). \quad (4)$$



(a) FFD volumes and reference axes



(b) Triangulated surface meshes

Fig. 3 Component-based geometry parameterization

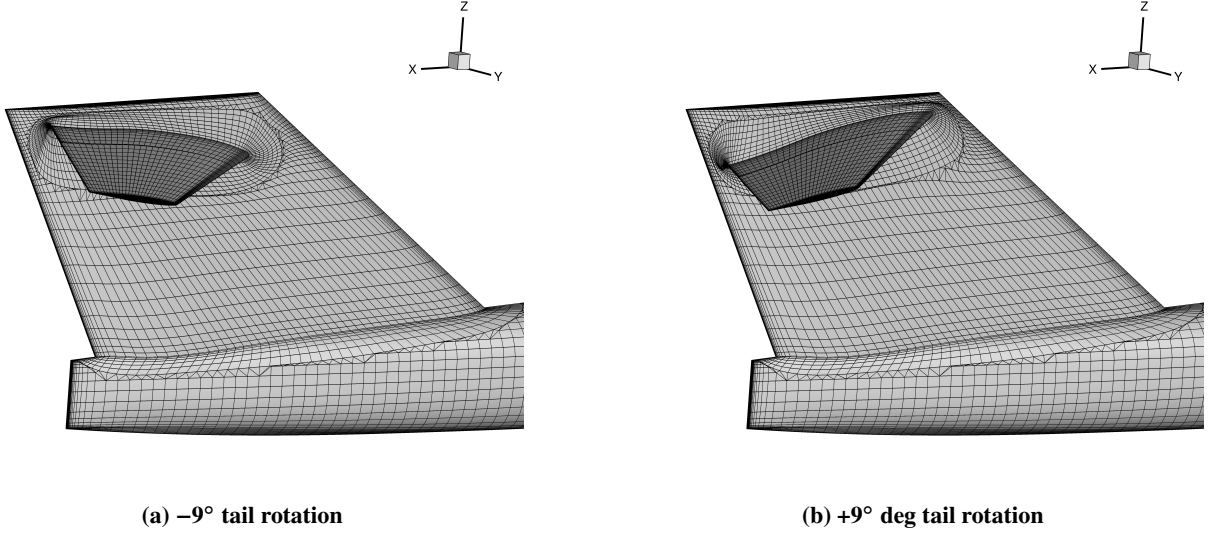


Fig. 4 Lower and upper bounds for the tail rotation

Substituting the definition of the static margin

$$K_n = h_{NP} - h_{CG}, \quad (5)$$

we can express the static margin in terms of aerodynamic forces and moments:

$$K_n = -\frac{C_{M_\alpha}}{C_{N_\alpha}}. \quad (6)$$

In previous work on CFD-based aircraft optimization [35–37], the static margin has been computed as

$$K_n = -\frac{C_{M_\alpha}}{C_{L_\alpha}} \quad (7)$$

This approach assumes that the angle of attack is small and that the drag is much smaller than the lift, both of which are true for a typical cruise condition. At off-design conditions, such as a supersonic aircraft in subsonic flight, these assumptions may be false. Replacing the lift with the normal force includes the effect of drag at high angles of attack.

For the static margin constraint, we need to compute both the stability derivatives and their gradients. Similar to prior work [35–37], we use a finite-difference approach to compute the stability derivatives. For example, we compute the pitching moment derivative as

$$C_{M_\alpha} = \frac{C_M|_{\alpha+\Delta\alpha} - C_M|_\alpha}{\Delta\alpha}, \quad (8)$$

where $\Delta\alpha = 0.1^\circ$ is a small perturbation in the angle of attack. This requires two flow solutions. By computing this slope as a finite difference, we can leverage the adjoint implementation in ADflow to compute the derivatives of C_{M_α} with respect to the design variables. More explicitly, these derivatives are computed as

$$\frac{dC_{M_\alpha}}{dx} = \frac{\frac{dC_M}{dx}|_{\alpha+\Delta\alpha} - \frac{dC_M}{dx}|_\alpha}{\Delta\alpha}, \quad (9)$$

where x is the vector of design variables and $\frac{dC_M}{dx}$ is computed using the adjoint method. We apply the same procedure to the lift and drag to compute the normal force coefficient and its gradients.

D. Optimized designs

We run optimizations both without the low-speed stability constraint (K_n unconstrained) and with the low-speed stability constraint (K_n constrained). We also run a pre-optimization to trim the baseline design. The pre-optimization

involves minimizing supersonic drag with only the angle of attack, tail rotation, and canard rotation as design variables. This provides a fair baseline supersonic drag value to compare the optimized results against. We run similar trim optimizations on the baseline and K_n unconstrained designs at the subsonic condition to evaluate their subsonic static margin.

Table 6 shows the supersonic drag, subsonic static margin, and trim variables for the baseline and optimized designs. The table also shows the feasibility (maximum constraint violation) and optimality for each optimization. The only design variable at its bound for either supersonic drag minimization problem is the wing vertical displacement. This variable is at its upper bound for the K_n unconstrained design and its lower bound for the K_n constrained design.

Table 6 Optimization results and convergence

	Baseline	K_n unconstrained	K_n constrained
Feasibility		1.9×10^{-5}	5.9×10^{-5}
Initial optimality		5.3×10^{-2}	9.0×10^{-2}
Final optimality		6.7×10^{-3}	1.9×10^{-2}
<i>Supersonic</i>			
Drag counts	398.0	320.4	339.1
Angle of attack	4.19°	8.19°	7.03°
Tail rotation	-5.64°	-3.09°	-2.28°
Canard rotation	6.79°	-4.46°	-1.99°
<i>Subsonic</i>			
Static margin	-31.4%	-33.7%	5.0%
Angle of attack	13.3°	18.8°	17.3°
Tail rotation	1.72°	4.02°	7.47°
Canard rotation	-0.42°	-5.50°	10.0°

The baseline design is unstable at the subsonic condition, which is expected because of the early pitch-up tendencies shown in Fig. 2c. The K_n unconstrained optimization decreases the drag from the baseline by 77.6 counts or 18.5% but is unstable with a more negative static margin than the baseline. This demonstrates the need for a low-speed stability constraint when performing supersonic shape optimization. The K_n constrained design is stable at the subsonic condition, showing that it is possible to use aerodynamic shape optimization to enforce subsonic stability for supersonic wing design. Relative to the K_n unconstrained design, there is a 5.8% drag penalty associated with adding the low-speed stability constraint.

The optimized designs are shown in Figs. 5 and 6. The K_n unconstrained design primarily uses twist to minimize the supersonic drag. The subsonic characteristics of the K_n unconstrained design are similar to the baseline because the washout is counteracted by the increased angle of attack at the subsonic condition. The two optimized designs have similar supersonic pressure and spanwise lift distributions. The difference in supersonic drag comes from the increased wing thickness of the K_n constrained design. The thickness is also responsible for the difference in pitch stability. Increasing the leading edge radius and wing thickness between 50% span and 80% span weakens the inboard leading edge vortex and improves pitch stability. This is consistent with trends reported in prior experimental and theoretical studies [1, 4, 5]. The decrease in lift near the wing break is compensated by increased camber and twist in the outboard section and more lift from the canard and tail. The same trends can be seen in the upper surface pressure coefficient contours (Fig. 7). The supersonic pressure contours are similar for both optimized designs. At the subsonic condition, the K_n constrained design has a weaker inboard leading edge vortex and a stronger outboard vortex than the K_n unconstrained design.

There are a few caveats to these results. First, the optimizations are not tightly converged. As a result, we cannot be confident that the results represent optimal designs. However, the constraints are satisfied to a relatively tight tolerance and the reduction in drag suggests that the optimizer made significant progress towards the optimum for both cases. The lack of reduction in optimality is related to difficulties in converging the adjoint equations tightly when using the zipper

mesh approach mentioned in Sec. II.B. This is particularly a concern for our mesh because the zippers account for a large percentage of the surface area compared to simpler configurations. Second, the subsonic canard rotation for the K_n unconstrained design hits the variable’s lower bound. This bound is set based on the largest angle that gives a valid mesh and is not physically relevant. It is possible that without this bound, the K_n unconstrained design’s subsonic static margin is closer to stable. However, the design is unlikely to satisfy the static margin constraint because this constraint is active for the K_n constrained design. Finally, the combined angle of attack and rotation angles for the canard and tail at subsonic conditions exceed 20 deg in some cases. This is likely pushing the limits of what RANS can accurately resolve, especially for the pitching moment. This is a fundamental limitation of steady CFD methods.

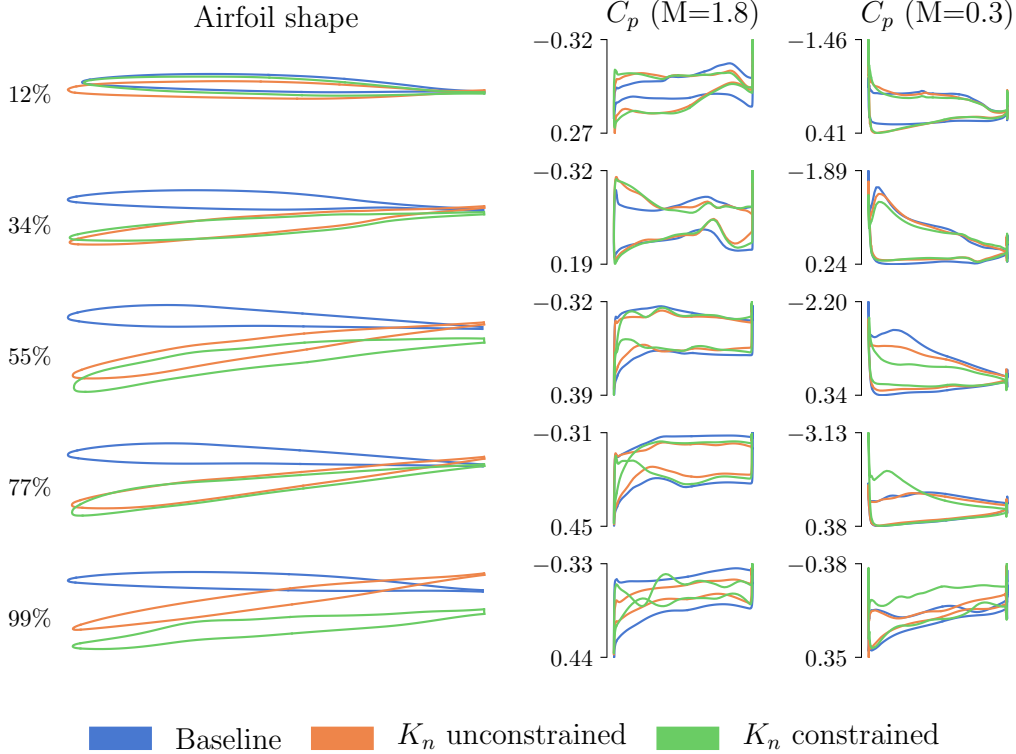


Fig. 5 Sectional shape and pressure distributions of baseline and optimized wing designs

IV. Conclusions

In this work, we use RANS-based aerodynamic shape optimization to study the low-speed stability of a supersonic transport configuration. We show that RANS captures the lift, drag, and pitching moment trends of the supersonic configuration at low-speed, high angle of attack conditions by comparing against experimental data. To parameterize the complete aircraft geometry, we use a component-based approach that works well with intersections. We minimize supersonic drag with and without a static margin constraint at a subsonic flight condition. The static margin computation differs from previous work on stability-constrained optimization by accounting for the effect of drag at high angles of attack. The baseline design and design optimized without a stability constraint are both unstable at subsonic speeds. The optimized design with the static margin constraint is stable at the subsonic condition as desired. Pitch stability is achieved by increasing the wing thickness and leading edge radius near the wing break. As a result, the stable design has 5.8% higher supersonic drag than the design optimized without a stability constraint. These results demonstrate that aerodynamic shape optimization is a valuable tool for capturing the trade-offs between supersonic performance and subsonic stability.

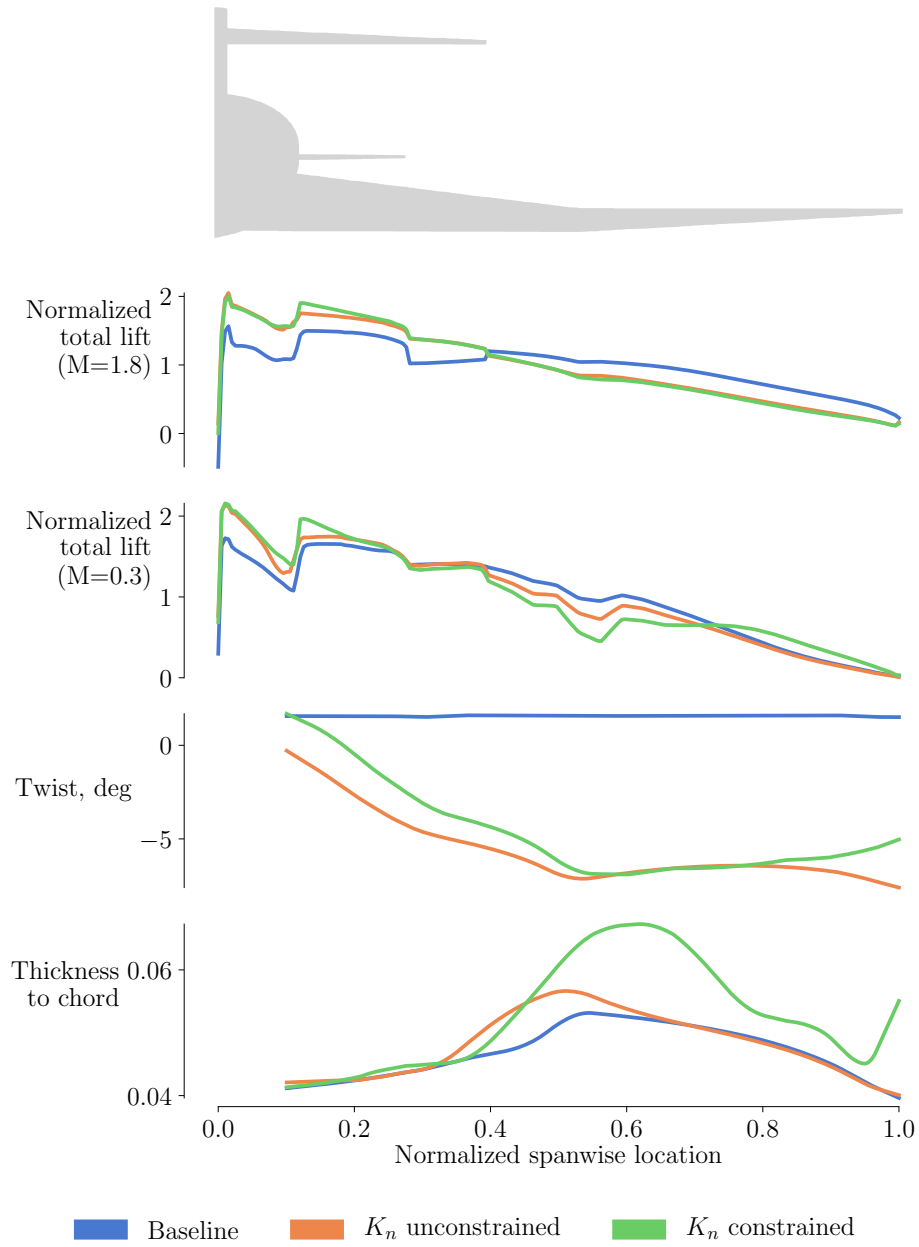


Fig. 6 Spanwise distributions of total lift, wing twist, and wing thickness for baseline and optimized designs

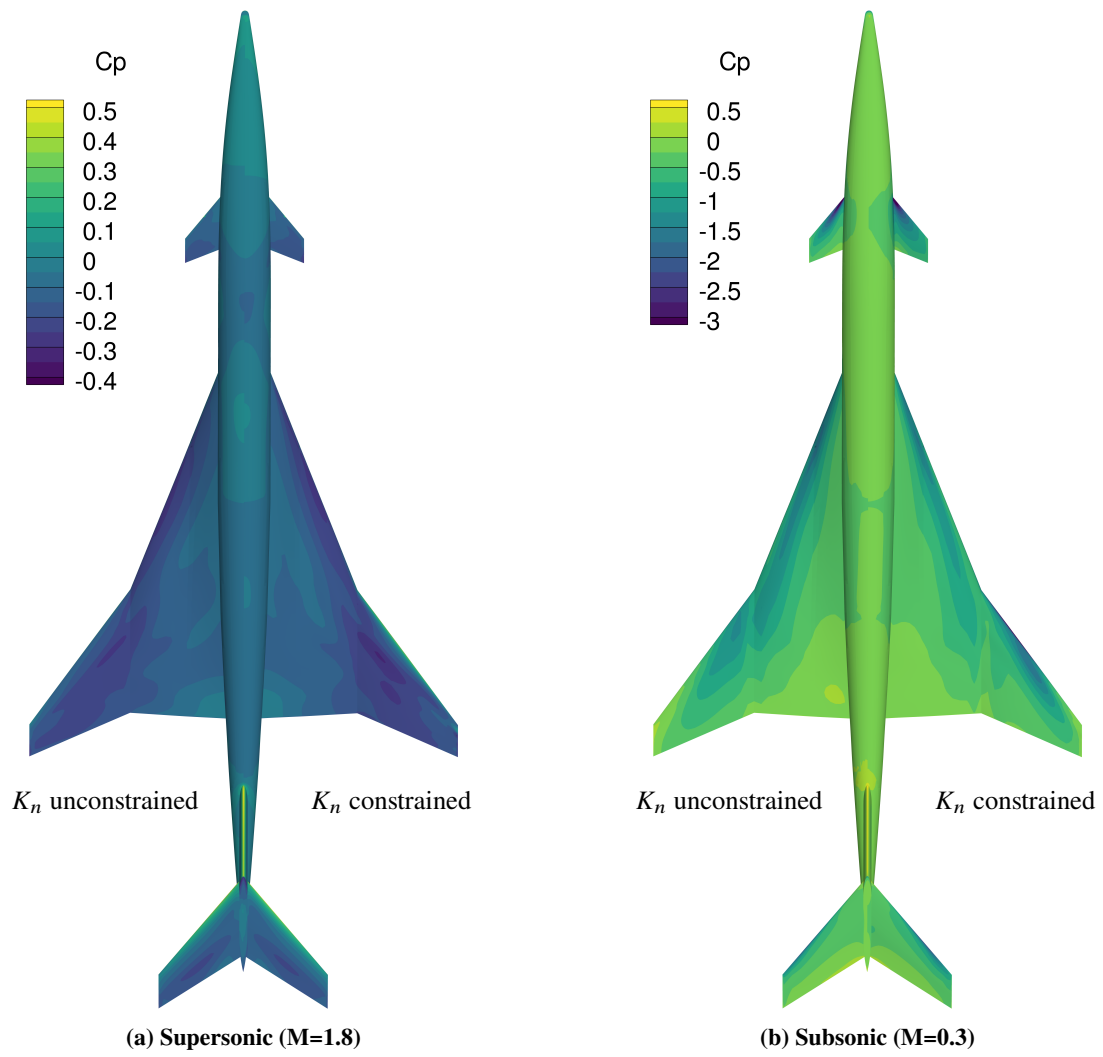


Fig. 7 Upper surface pressure contours for optimized designs

Acknowledgments

We thank Anil Yildirim and Yingqian Liao for their advice on overset meshing and geometry parameterization. We also thank our collaborators at the University of Washington (particularly Nick Mavriplis) for providing the aircraft geometry and wind tunnel data. This work was supported by NASA under the University Leadership Initiative program ‘Supersonic Configurations at Low Speeds’ with Sarah Langston as the NASA technical grant monitor. S. Seraj was also supported by the Natural Sciences and Engineering Research Council of Canada (NSERC), [funding reference number PGSD3 - 545678 - 2020]. Computational resources were provided by the NASA High-End Computing (HEC) Program through the NASA Advanced Supercomputing (NAS) Division at Ames Research Center.

References

- [1] Nelson, C. P., “Effects of Wing Planform on HSCT Off-design Aerodynamics,” *Proceedings of the 10th Applied Aerodynamics Conference*, 1992. doi:10.2514/6.1992-2629.
- [2] Luckring, J. M., “The discovery and prediction of vortex flow aerodynamics,” *The Aeronautical Journal*, Vol. 123, No. 1264, 2019, pp. 729—804. doi:10.1017/aer.2019.43.
- [3] Benoliel, A. M., and Mason, W. H., “Pitch-up characteristics for HSCT class planforms: Survey and estimation,” *12th Applied Aerodynamics Conference*, 1994. doi:10.2514/6.1994-1819.
- [4] Kulfan, R. M., “Wing Airfoil Shape Effects on the Development of Leading Edge Vortices,” *5th Atmospheric Flight Mechanics Conference for Future Space Systems*, 1979. doi:10.2514/6.1979-1675.
- [5] Kulfan, R. M., “Wing Geometry Effects on Leading Edge Vortices,” *Aircraft Systems and Technology Meeting*, 1979. doi:10.2514/6.1979-1872.
- [6] Cliff, S. E., Reuther, J. J., Saunders, D. A., and Hicks, R. M., “Single-Point and Multipoint Aerodynamic Shape Optimization of High-Speed Civil Transport,” *Journal of Aircraft*, Vol. 38, No. 6, 2001, pp. 997–1005.
- [7] Carrier, G., “Single and Multi-Point Aerodynamic Optimizations of a Supersonic Transport Aircraft Wing Using Optimization Strategies Involving Adjoint Method and Genetic Algorithm,” *Proceedings of ERCOFTAC Workshop*, 2006.
- [8] Bons, N. P., Martins, J. R. R. A., Mader, C. A., McMullen, M., and Suen, M., “High-fidelity Aerostructural Optimization Studies of the Aerion AS2 Supersonic Business Jet,” *Proceedings of the AIAA Aviation Forum*, 2020. doi:10.2514/6.2020-3182.
- [9] Mangano, M., and Martins, J. R. R. A., “Multipoint Aerodynamic Shape Optimization for Subsonic and Supersonic Regimes,” *Journal of Aircraft*, 2021. doi:10.2514/1.C036216.
- [10] Dudley, J., Huang, X., MacMillin, P., Grossman, B., Haftka, R., and Mason, W., “Multidisciplinary Optimization of the High-speed Civil Transport,” *33rd Aerospace Sciences Meeting & Exhibit*, 1995. doi:10.2514/6.1995-124.
- [11] Crisafulli, P., Kaufman, M., Giunta, A., Mason, W., Grossman, B., Watson, L., and Haftka, R., “Response surface approximations for pitching moment including pitch-up in the MDO design of an HSCT,” *6th Symposium on Multidisciplinary Analysis and Optimization*, 1996. doi:10.2514/6.1996-4136.
- [12] Li, W., and Geiselhart, K., “Multidisciplinary Design Optimization of Low-Boom Supersonic Aircraft with Mission Constraints,” *AIAA Journal*, Vol. 59, No. 1, 2021, pp. 165–179. doi:10.2514/1.J059237.
- [13] Li, W., and Geiselhart, K., “Integration of Low-Fidelity MDO and CFD-Based Redesign of Low-Boom Supersonic Transports,” *AIAA Journal*, Vol. 59, No. 10, 2021, pp. 3923–3936. doi:10.2514/1.J060368.
- [14] Ting, K.-Y., Mavriplis, N., Soltani, R., Soltani, R., and Livne, E., “Supersonic Configurations at Low Speeds (SCALOS): Introduction to the Program and the Year-I 2020-2021 Configurations,” *AIAA SciTech Forum*, 2022.
- [15] Mavriplis, N., Ting, K.-Y., Soltani, R., Soltani, R., and Livne, E., “Supersonic Configurations at Low Speeds (SCALOS): Test / Analysis Correlation Studies,” *AIAA SciTech Forum*, 2022.
- [16] Mader, C. A., Kenway, G. K. W., Yildirim, A., and Martins, J. R. R. A., “ADflow: An open-source computational fluid dynamics solver for aerodynamic and multidisciplinary optimization,” *Journal of Aerospace Information Systems*, Vol. 17, No. 9, 2020, pp. 508–527. doi:10.2514/1.I010796.
- [17] Spalart, P., and Allmaras, S., “A One-Equation Turbulence Model for Aerodynamic Flows,” *La Recherche Aerospatiale*, Vol. 1, 1994, pp. 5–21.

- [18] Chan, W., Gomez, R., Rogers, S., and Buning, P., “Best Practices in Overset Grid Generation,” *32nd AIAA Fluid Dynamics Conference and Exhibit*, American Institute of Aeronautics and Astronautics, 2002. doi:[10.2514/6.2002-3191](https://doi.org/10.2514/6.2002-3191).
- [19] Secco, N., Kenway, G. K. W., He, P., Mader, C. A., and Martins, J. R. R. A., “Efficient Mesh Generation and Deformation for Aerodynamic Shape Optimization,” *AIAA Journal*, Vol. 59, No. 4, 2021, pp. 1151–1168. doi:[10.2514/1.J059491](https://doi.org/10.2514/1.J059491).
- [20] Chan, W. M., and Steger, J. L., “Enhancements of a three-dimensional hyperbolic grid generation scheme,” *Applied Mathematics and Computation*, Vol. 51, No. 2–3, 1992, pp. 181–205. doi:[10.1016/0096-3003\(92\)90073-A](https://doi.org/10.1016/0096-3003(92)90073-A).
- [21] Chan, W. M., “Enhancements to the Hybrid Mesh Approach to Surface Loads Integration on Overset Structured Grids,” *19th AIAA Computational Fluid Dynamics*, 2009. doi:[10.2514/6.2009-3990](https://doi.org/10.2514/6.2009-3990).
- [22] Kenway, G. K. W., Secco, N., Martins, J. R. R. A., Mishra, A., and Duraisamy, K., “An Efficient Parallel Overset Method for Aerodynamic Shape Optimization,” *Proceedings of the 58th AIAA/ASCE/AHS/ASC Structures, Structural Dynamics, and Materials Conference, AIAA SciTech Forum*, Grapevine, TX, 2017. doi:[10.2514/6.2017-0357](https://doi.org/10.2514/6.2017-0357).
- [23] Martins, J. R. R. A., “Perspectives on Aerodynamic Design Optimization,” *AIAA SciTech Forum*, AIAA, Orlando, FL, 2020. doi:[10.2514/6.2020-0043](https://doi.org/10.2514/6.2020-0043).
- [24] Yildirim, A., Kenway, G. K. W., Mader, C. A., and Martins, J. R. R. A., “A Jacobian-free approximate Newton–Krylov startup strategy for RANS simulations,” *Journal of Computational Physics*, Vol. 397, 2019, p. 108741. doi:[10.1016/j.jcp.2019.06.018](https://doi.org/10.1016/j.jcp.2019.06.018).
- [25] Kenway, G. K. W., Mader, C. A., He, P., and Martins, J. R. R. A., “Effective Adjoint Approaches for Computational Fluid Dynamics,” *Progress in Aerospace Sciences*, Vol. 110, 2019, p. 100542. doi:[10.1016/j.paerosci.2019.05.002](https://doi.org/10.1016/j.paerosci.2019.05.002).
- [26] Sederberg, T. W., and Parry, S. R., “Free-form Deformation of Solid Geometric Models,” *SIGGRAPH Comput. Graph.*, Vol. 20, No. 4, 1986, pp. 151–160. doi:[10.1145/15886.15903](https://doi.org/10.1145/15886.15903).
- [27] Kenway, G. K., Kennedy, G. J., and Martins, J. R. R. A., “A CAD-Free Approach to High-Fidelity Aerostructural Optimization,” *Proceedings of the 13th AIAA/ISSMO Multidisciplinary Analysis Optimization Conference*, Fort Worth, TX, 2010. doi:[10.2514/6.2010-9231](https://doi.org/10.2514/6.2010-9231).
- [28] Luke, E., Collins, E., and Blades, E., “A Fast Mesh Deformation Method Using Explicit Interpolation,” *Journal of Computational Physics*, Vol. 231, No. 2, 2012, pp. 586–601. doi:[10.1016/j.jcp.2011.09.021](https://doi.org/10.1016/j.jcp.2011.09.021).
- [29] Wu, N., Kenway, G., Mader, C. A., Jasa, J., and Martins, J. R. R. A., “pyOptSparse: A Python framework for large-scale constrained nonlinear optimization of sparse systems,” *Journal of Open Source Software*, Vol. 5, No. 54, 2020, p. 2564. doi:[10.21105/joss.02564](https://doi.org/10.21105/joss.02564).
- [30] Gill, P. E., Murray, W., and Saunders, M. A., “SNOPT: An SQP Algorithm for Large-Scale Constrained Optimization,” *SIAM Review*, Vol. 47, No. 1, 2005, pp. 99–131. doi:[10.1137/S0036144504446096](https://doi.org/10.1137/S0036144504446096).
- [31] Welge, H. R., Bonet, J., Magee, T., Chen, D., Hollowell, S., Kutzmann, A., Mortlock, A., Stengle, J., Nelson, C., Adamson, E., Baughcum, S., Britt, R. T., Miller, G., and Tai, J., “N+2 Supersonic Concept Development and Systems Integration,” Tech. Rep. NASA/CR-2010-216842, NASA, Langley Research Center, Hampton, VA, 2010.
- [32] Morgenstern, J., Buonanno, M., Yao, J., Murugappan, M., Paliath, U., Cheung, L., Malcevici, I., Ramakrishnan, K., Pastouchenko, N., Wood, T., Martens, S., Viars, P., Tersmette, T., Lee, J., Simmons, R., Plybon, D., Alonso, J., Palacios, F., Lukaczyk, T., and Carrier, G., “Advanced Concept Studies for Supersonic Commercial Transports Entering Service in the 2018-2020 Period Phase 2,” Tech. Rep. NASA/CR—2015-218719, NASA, Glenn Research Center, Cleveland, OH, 2015.
- [33] Yildirim, A., Mader, C. A., and Martins, J. R. R. A., “A Surface Mesh Deformation Method Near Component Intersections for High-Fidelity Design Optimization,” *Engineering with Computers*, 2021. doi:[10.1007/s00366-020-01247-w](https://doi.org/10.1007/s00366-020-01247-w).
- [34] Secco, N. R., Jasa, J. P., Kenway, G. K. W., and Martins, J. R. R. A., “Component-based Geometry Manipulation for Aerodynamic Shape Optimization with Overset Meshes,” *AIAA Journal*, Vol. 56, No. 9, 2018, pp. 3667–3679. doi:[10.2514/1.J056550](https://doi.org/10.2514/1.J056550).
- [35] Mader, C. A., and Martins, J. R. R. A., “Stability-Constrained Aerodynamic Shape Optimization of Flying Wings,” *Journal of Aircraft*, Vol. 50, No. 5, 2013, pp. 1431–1449. doi:[10.2514/1.C031956](https://doi.org/10.2514/1.C031956).
- [36] Kenway, G. K. W., and Martins, J. R. R. A., “Multipoint High-Fidelity Aerostructural Optimization of a Transport Aircraft Configuration,” *Journal of Aircraft*, Vol. 51, No. 1, 2014, pp. 144–160. doi:[10.2514/1.C032150](https://doi.org/10.2514/1.C032150).
- [37] Reist, T. A., and Zingg, D. W., “High-Fidelity Aerodynamic Shape Optimization of a Lifting-Fuselage Concept for Regional Aircraft,” *Journal of Aircraft*, Vol. 54, No. 3, 2017, pp. 1085–1097. doi:[10.2514/1.C033798](https://doi.org/10.2514/1.C033798).